Chapter 2: Methods and Materials

This chapter will outline the experimental methods used in this work. The tested materials are discussed in Section 2.1 along with the salts and the composition of the salt mixtures used. The preparation of the testing samples will also be discussed in Section 2.2. The general setup for the corrosion testing is outlined in Section 2.3, and this section also provides more detail of the four different corrosion tests conducted in this work. Finally, the different analysis techniques will be described in Section 2.4.

2.1 Materials

2.1.1: Stainless steel

Three different stainless steels are investigated, along with iron, and their elemental compositions are given in Table 2.1.

Table 2.1: Elemental composition (wt. %) of the three stainless steels and the iron sample used in this work determined by ICP-OES and combustion methods by Element Materials Technology. All values for iron have been calculated by difference.

	Fe	**Cr**	**Ni**	**Mn**	**Mo**	**Si**	**C**	**P**	**S**	**N**
Stainless steel 316L	69.59	16.36	10.14	1.35	2.13	0.37	0.02	0.033	<0.003	
Stainless steel 304L	71.23	18.31	8.28	1.46	0.42	0.26	0.024	0.018	<0.003	
LDX2101	71.20	21.42	1.55	4.69	0.21	0.68	0.021	0.013	<0.003	0.21
Iron	99.69	0.04	0.03	0.15	<0.01	0.02	0.03	0.01	0.022	

Stainless steels generally have a chromium content of at least 10.5 wt. %, they are known for their corrosion resistance as the high chromium content enables a chromium oxide (Cr_2O_3) layer to form in air, which then protects the alloy in atmospheric or aqueous environments [1]. Although it was stated in Section 1.4 that passivating oxide layers are unstable in a molten salt environment, chemical compatibility has been seen in clean FLiBe [2, 3].

The 300 series of stainless steels is austenitic in nature, with a face centred cubic crystal structure. Nickel or manganese is added to ensure that the FCC phase is maintained [1].

The two stainless steel samples (304L and 316L) were temper annealed and received as sheets from Advent Research Materials. LDX2101 was received as sheet offcuts from Harvey Steel Lintels Limited,

the samples are hot rolled, heat treated and pickled. Iron was also received from Advent Research Materials.

2.1.2: Salts

Ternary and binary eutectic salts are used in this work, and Table 2.2 along with Figure 2. 1 show the basic properties of the two mixtures along with their phase diagrams. Components in a eutectic do not chemically react with one another, but their combination results in a lower melting temperature compared to their constituent parts. This allows corrosion testing to be conducted at a significantly reduced temperature [4].

Table 2.2: Basic properties of the two eutectic mixtures utilised in this work [5, 6]

	Ternary	**Binary**
Salt	NaCl-LiCl-KCl	NaCl-KCl
wt. %	8.74 :42.63: 48.63[5]	43.94:56.06 (50:50 mol %)[6]
Eutectic temperature °C	429	645

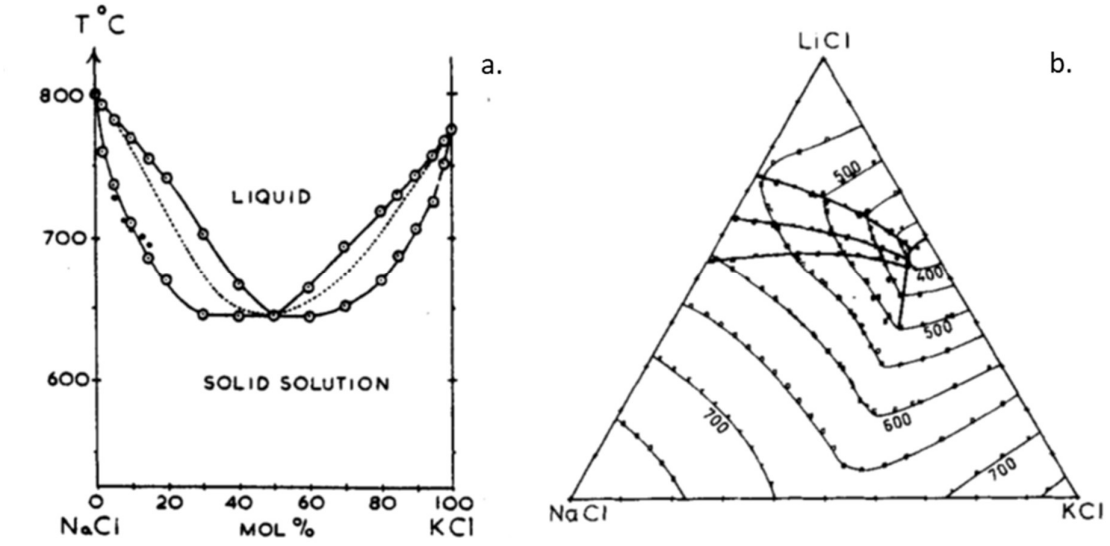

Figure 2.1: Phase diagram for NaCl-KCl (left) and NaCl-LiCl-KCl (right) (sourced from Coleman and Lacy, and Lin et al., respectively) [6, 7].

The mass of each of the constituent salts required to make 60 cm^3 was determined from the phase diagram, Figure 2.1, and weighed on a four decimal place balance. Sodium chloride was sourced from Sigma Aldrich, it is ACS reagent grade and has a purity of >99%. Lithium chloride and potassium chloride were both sourced from Alfa Aesar with a purity of >98% and 99%. The grade is not stated. This information along with melting temperatures can be seen in Table 2.3.

Table 2.3: Information regarding the purity, sourcing and melting temperature of each individual salt [8-10].

Salt	wt.% in eutectic	Melting temperature, °C	Purity	Grade	Source
NaCl	8.740%	801	>99%	ACS reagent	Sigma Aldrich
LiCl	42.63%	605	>98%	Not stated	Alfa Aesar
KCl	48.63%	770	99%	Not stated	Alfa Aesar

2.2 Preparation of Testing Specimens

All the samples used in this work were received as sheets or coupons and were prepared to a common standard prior to experimental work. The samples were polished using a method recommended by Buehler for stainless steel [11] as outlined in Table 2.4. As a uniform finish was deemed acceptable for the samples undergoing corrosion tests they were polished to a 3 µm finish. This gave the sample a mirror like shine, with visible scratches, these can be seen in Figure 2.2.

Table 2.4: Polishing techniques.

Corrosion testing
Sectioning
Grinding 240 grit paper
Polishing to a 9 µm finish
Polishing to a 3 µm finish
Cleaning

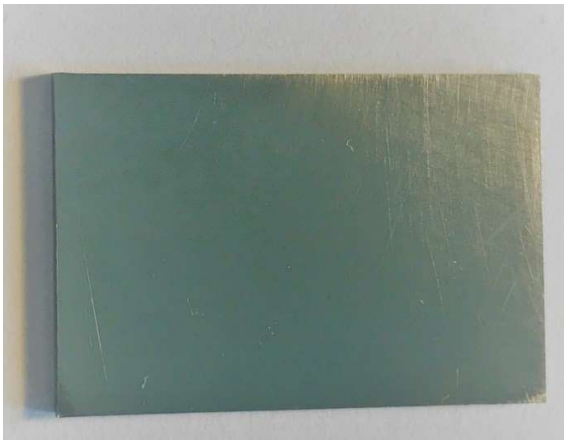

Figure 2.2: Stainless steel 316L after polishing.

Samples measuring below 125 mm were cut using an IsoMet precision saw and a ferrous blade. A soft start was used to prevent the blade breaking, with a speed of 2500 rpm and a feed rate of 1.2 mm/min, which was gradually increased during the cutting process. Each sample was sized between 15-30 mm by 15-20 mm depending on the availability of material.

The samples were ground and polished using an Automet 250; as the samples used for corrosion testing could not be mounted, a central force on a planar mounting head was used to prepare the samples. An initial load of 27 N was used, but it proved difficult to obtain a planar surface as bevels formed due to the method of mounting. To overcome this issue coarser grinding paper (120 grit) was utilised along with a larger load, 96 N. Once a planar surface was obtained 240 grit paper was used and the samples were polished to a 3 µm finish.

Once the samples had been prepared they were cleaned in a sonic bath using isopropanol for five minutes.

2.3: Corrosion Testing

Corrosion testing took place within a fume hood using a top loader Elite Furnace with a maximum temperature of 1200°C. Four different sets of experiments were run, and these are discussed in more detail in Section 2.3.1. The samples were washed in a sonic bath using isopropanol for five minutes and the weight of each sample was noted. The required mass for each of the constituent salts was determined by the phase diagrams, shown in Figure 2.1, and were mixed in an alumina crucible and the stainless steel sample added. The crucible was placed into the furnace at room temperature in atmospheric conditions and was initially heated to 120°C for an hour to evaporate any residual water, prior to being heated to the predetermined temperature at a rate of 2°C/min, and left for the scheduled time, which ranged from 24-1000 hours. It was found by Sridharan and Allen [12] that corrosion of materials in a molten fluoride was higher in a quartz container compared to alumina. It has been theorised that SiO_2 from the quartz container reacts with water and the fluoride salt to give hydrofluoric acid (HF), which leads to enhanced corrosion, therefore alumina crucibles were utilised [12]. The different conditions for each of the samples are discussed in Section 2.3.1. The different salt mixtures and the samples are discussed further in Section 2.1. Once testing was complete the furnace was cooled to room temperature and the alumina crucibles removed. The samples were subsequently removed by dissolving the salt using distilled water. The samples were air-dried and weighed to determine % mass change.

All the experiments followed the procedure described, with the salt, temperature, material and time frame varying, and these are discussed in further detail in Section 2.3.1 .

2.3.1: Experiments

2.3.1.1: Baseline Tests

The initial baseline tests utilised a LiCl-KCl-NaCl eutectic salt, whose composition and properties are given in Table 2.2, and stainless steel 316L, details of the composition are given in Table 2.1. The experiment was run at 600°C for one day, and the aim of this work was to determine if stainless steel 316L could withstand the extreme environment and temperature used in this work. As this test was originally intended to determine the viability of stainless steel 316L within the environment the mass change of the sample was not measured.

2.3.1.2: Stainless Steel 316L Tests

Once the baseline tests proved that stainless steel 316L could withstand the high temperature molten salt environment, further tests were conducted on stainless steel 316L. These were run in the same conditions as the baseline tests, but for different time ranges; one, three, four and six weeks. These times were selected as it was stated by Richardson et al. [13] that in dynamic and static testing on Inconels, stainless steels and Hastelloys in a molten fluoride environment, a levelling off of the reaction rate is seen after 500 hours, and three weeks is approximately 500 hours. The tests at one, four and six weeks were added to give a clearer picture of the mechanism.

2.3.1.3: Lithium Tests

It was also evident from the stainless steel 316L tests that lithium was an important constituent of the corrosion product when stainless steel is immersed in a molten salt. These tests were conducted to determine the role lithium plays in the corrosion of stainless steel. These tests used stainless steel 316L for one, three and four weeks and utilised a ternary (NaCl-KCl-LiCl) and a binary (NaCl-KCl) eutectic. As the melting temperature of the binary eutectic (654°C) is higher than the temperatures used in the previous tests (600°C), the tests were run at 700°C.

2.3.1.4: Compositional Tests

From the results obtained in previous tests, it was determined that chromium is a major component of the corrosion process. The elemental compositions of numerous different alloys were assessed and it was decided that two further alloys would be tested to study the effect chromium content has on

the sample; LDX2101 and stainless steel 304L were chosen, along with iron, and further information on each of these is given in Section 2.1.1. LDX2101 is a duplex stainless steel and has a chromium content which is approximately 24% higher than stainless steel 316L (21.42 wt. % compared to 16.36 wt. %). Stainless steel 304L is similar to 316L but also has a higher chromium content (28.31 wt. % compared to 16.36 wt. %). The full compositions can be seen in Table 2.1.

These tests were run at 600°C for one, three and four weeks and utilised a ternary eutectic salt, NaCl-LiCl-KCl, whose composition is given in Table 2.2.

2.4: Analysis

Four different alloy compositions are used in this work and each one required elemental analysis. To do this inductively coupled plasma optical emission spectroscopy (ICP-OES) was utilised in combination with traditional combustion methods.

2.4.1: Inductively Coupled Plasma Optical Emission Spectroscopy (ICP-OES)

Inductively coupled plasmas (ICP) can be used to determine the composition of materials, by creating ions that emit characteristic signals for each individual element. The sample is subjected to temperatures high enough to cause dissociation and ionisation. The atoms and ions in their excited state decay back to their ground state through the emission of quantised electromagnetic radiation. The intensity of the emitted radiation can be measured and used to identify elements within the sample and their concentrations [14]. The ICP-OES is made up of two parts; the excitation source and an optical emission spectrometer.

A schematic of an ICP-OES is shown in Figure 2.3 and shows the different components that make up the machine. To introduce the sample into the ICP it generally has to be a liquid, therefore it is necessary to dissolve all solid samples. Sometimes lasers are used to convert the solid sample into a gas and no liquid is required. In this work the sample is digested in an acid mixture containing HCl, HNO_3, HF and H_2O. This liquid can then be nebulised into an aerosol making it easier to transfer the sample into the centre of the plasma, this is generally done via pneumatic forces, using a high speed jet of gas, usually argon. Once the aerosol is formed it is transported directly into the centre of a quartz torch. As only small particles are required a spray chamber is used. The spray chamber will remove any large droplets from the aerosol, and only allow droplets with a diameter of 10 µm or smaller to pass through to the torch, this makes up about 1-5% of the aerosol that is initially added into the chamber [15, 16].

The torch used to create the plasma consists of three concentric quartz tubes for argon and aerosol injections. The sample is injected directly into the centre of the torch; there is uniform heating and a contact time of approximately 30 seconds [14]. The plasma has numerous functions once the aerosol is added. Firstly the solvent (deionised water, in this work) in which the sample is dissolved needs to be removed, leaving the sample as microscopic particles. These particles are then decomposed into a gas of individual molecules which are then atomised. Once the sample is atomised within the plasma, the plasma can either ionise or excite the atoms. A radio frequency generator surrounds the torch and provides the power to create the plasma discharge, the power supplied ranges from 700-1500 W and oscillates the coil generating electrical and magnetic fields. When a spark is added electrons are stripped from the argon and accelerated by the magnetic field, thus forming plasma. Plasma is defined as a state of matter which has numerous charged ions (>1%) in addition to neutral atoms and molecules. They can conduct electricity and are also affected by magnetic fields [17]. The addition of energy to these ions via the coil is known as inductive coupling. High energy electrons collide with argon and strip off more electrons leading to a chain reaction, giving rise to the formation of an inductively coupled plasma discharge, itself consisting of argon atoms / ions and electrons. The argon ions and free electrons are further agitated by the RF field leading to temperatures within the plasma reaching 8000-10,000 K [14, 16, 18].

The radiation emitted from the sample is then collected using a focusing optic. As excited species in the plasma emit light at numerous different wavelengths the emission is classed as polychromatic. It is essential to separate these into individual wavelengths which is done by using a diffraction grating, usually a monochromator, which measures one wavelength at a time. When light strikes the grating it is diffracted at an angle which is dependent on its wavelength. Generally the longer the wavelength the higher the angle of diffraction. The emitted radiation is then detected using a photosensitive detector [14, 15].

To determine the composition of an element, standard solutions of known concentrations are tested to give a plot of intensity vs concentration, a calibration curve. These are compared to the intensity measured from the sample and once the concentration is known it is possible to determine the wt. % of each element within a sample [15].

Although ICP-OES is a highly accurate way to measure the elemental composition of a sample there are also disadvantages associated with it. Firstly, it is a destructive technique as the sample is required to be liquid and nebulised. It is also not possible to identify argon, whilst other elements require special requirements before they can be detected. These include unstable or radioactive samples, and

the halogens; fluorine, chlorine and bromine which require special optics as they have short wavelengths and high excitation energies [16]. Chlorine is particularly difficult as it is next to argon on the periodic table, making the signal hard to detect.

As aqueous environments tend to be used, hydrogen and oxygen are also difficult to detect. There is also the possibility of air being present within the system and therefore oxygen, nitrogen, hydrogen and carbon can be problematic to trace [14].

The ICP-OES instrument used in this work is a Thermo Scientific ICAP6000.

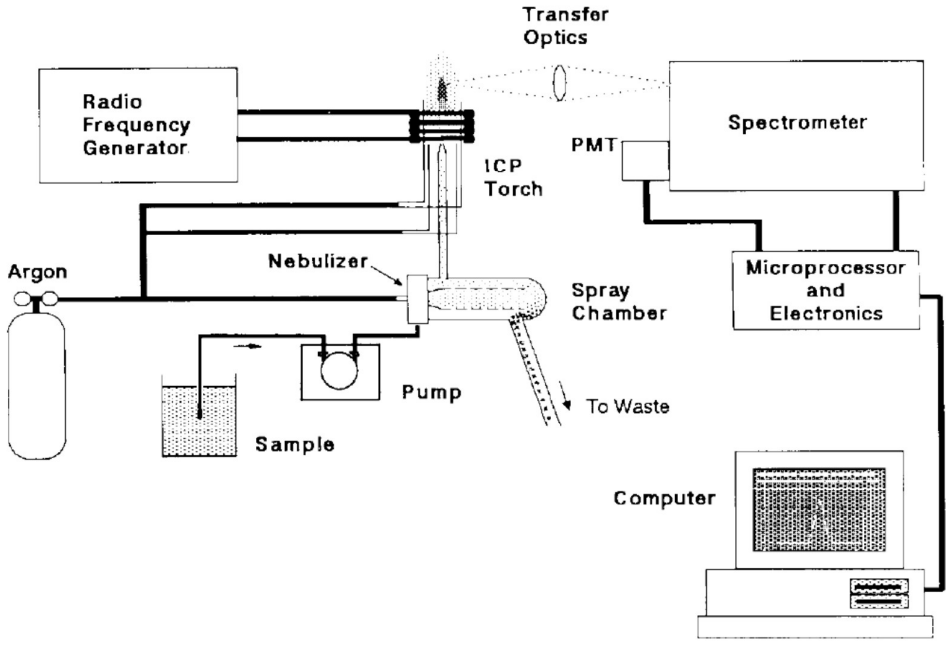

Figure 2.3: Schematic of an ICP-OES, reproduced from Boss and Fredeen [14].

2.4.2: Combustion Methods

As previously mentioned it is difficult to obtain ICP-OES data for elements that may accidentally be added to the plasma via air, therefore combustion methods based on dynamic flash combustion were also used to determine the presence of hydrogen, carbon, sulphur and nitrogen; a schematic is shown in Figure 2.4. Approximately 1 g of the sample is ground down using a clean file to prevent contamination, the elements are converted to their oxides i.e. carbon dioxide, water, nitrogen dioxide and sulphur dioxide, and added into a furnace running at approximately 1000°C. This converts the elements into their combustion products. The oxides are removed from the furnace via an inert carrier gas such as helium and passed over heated copper at approximately 600°C. This removes any oxygen

that has not reacted and also converts oxides of nitrogen to nitrogen gas. The gas is then passed through absorbent traps to leave carbon dioxide, sulphur dioxide and nitrogen gas. The gases are then detected by gas chromatography followed by quantification using thermal conductivity detection [19].

This work uses a LECO CS844ES instrument.

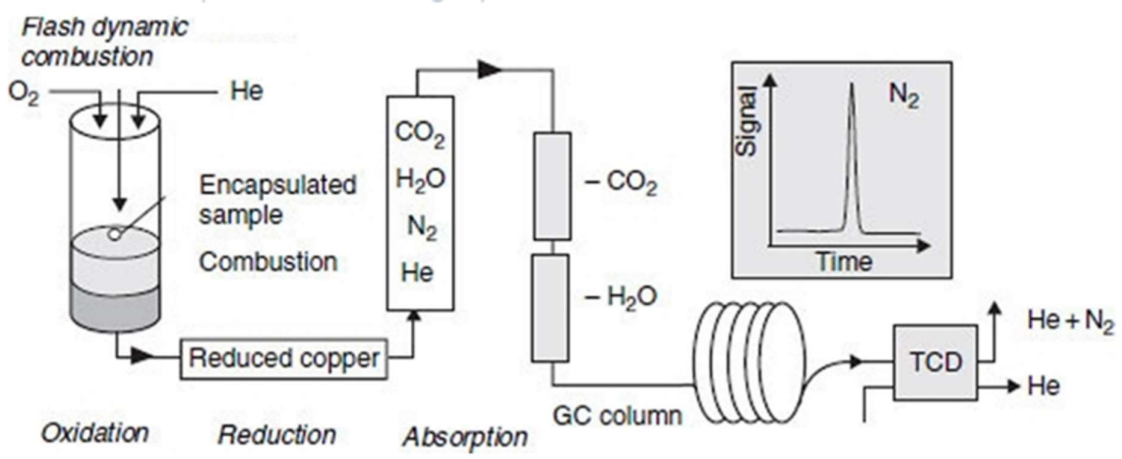

Figure 2.4: Schematic of dynamic flash combustion, reproduced from Rouessac and Rouessac [20].

2.4.3: X-Ray Diffraction (XRD)

X-rays have short wavelengths/high frequencies and are generated when matter is bombarded by high energy particles including photons. X-rays can be utilised for phase identification as their short wavelengths are similar to the size of an atom.

X-ray diffraction (XRD) is commonly used to investigate crystalline materials, as each system has a characteristic pattern formed by coherent elastic scattering of X-rays from electrons within the material, which can be used for its identification [21].

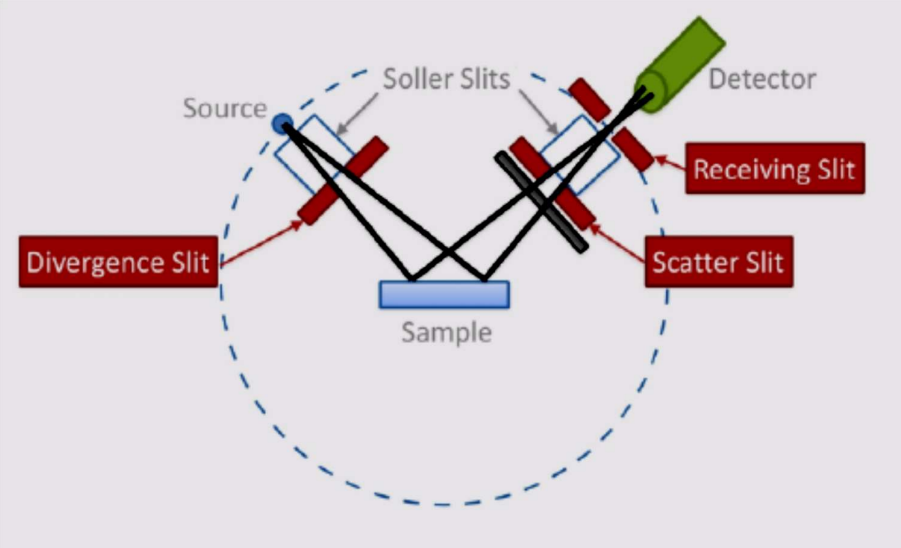

Figure 2.5: Schematic of a XRD instrument, reproduced from N. Reeves-McLaren [22].

X-rays are produced in a sealed X-ray tube by hitting a metal target with accelerated electrons from a hot tungsten filament; in this work, copper was used (λ = 0.1541 nm) [23].

Electrons collide with the metal target, giving rise to ionisation and ejection of electrons. The resultant vacancies are filled by electrons from higher shells, dropping down, emitting quantised X-rays as they do so. It is possible to generate X-rays from the transition of electrons to the K, L and M shells with each shell having numerous discrete energy levels, this is shown in Figure 2.6. A transition from L to K gives rise to K_{α} radiation, and a transition from M to K gives rise to K_{β} radiation. As each shell is made up of orbitals, which are at slightly different energies, it is possible to get transitions from the same shell but with slightly different energies, these are labelled e.g. $K_{\alpha 1}$, $K_{\alpha 2}$, $K_{\beta 1}$, $K_{\beta 2}$, $K_{\beta 3}$ [24].

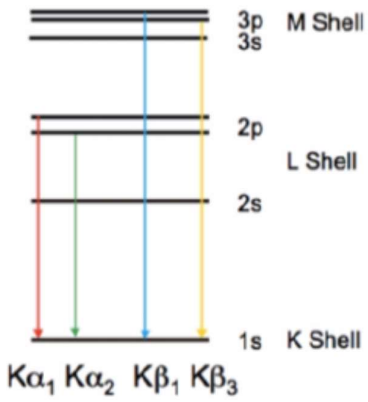

Figure 2.6: Some possible electron transitions [22].

Once generated, the X-rays exit the tube through a thin (generally 0.125 μm) beryllium window. Beryllium is used as it has a low atomic number and therefore X-ray absorption, especially in such a thin window, is not significant [25].

Primary optics control the beam before it interacts with the sample, generally preventing axial divergence, which can lead to peak shifts. Divergence slits prevent any height divergence in the plane of diffraction, this determines the size of the X-ray beam hitting the sample and increases the resolution.

Post sample secondary optics are between the sample and the detector, which contains anti-scatter slits, with a similar design and operation to divergence slits. These are followed by receiving slits which remove some of the diffuse scattering. Finally, a filter (e.g. nickel, for a copper radiation source) is used to remove K_β contributions [22, 23].

There are several different types of X-ray detectors, which include scintillation counters, imaging plates, and position sensitive detectors. The Bruker D2 Phaser instrument which was used in this work uses a LYNXEYE 1D detector (PSD) [23] with a step size of 0.02°.

Generally destructive interference will occur whereby the combining waves are out of phase and therefore there is no resultant energy leaving the solid sample. However, in a crystal with a regular pattern, it is possible to obtain constructive interference, whereby the waves are in phase. When the X-ray beam interacts with the crystal structure, part of it can diffract back, and Bragg's law states that when the path difference is an integer number of wavelengths, constructive interference will occur. This is shown in Figure 2.7 and the equation is given in Equation 2.1.

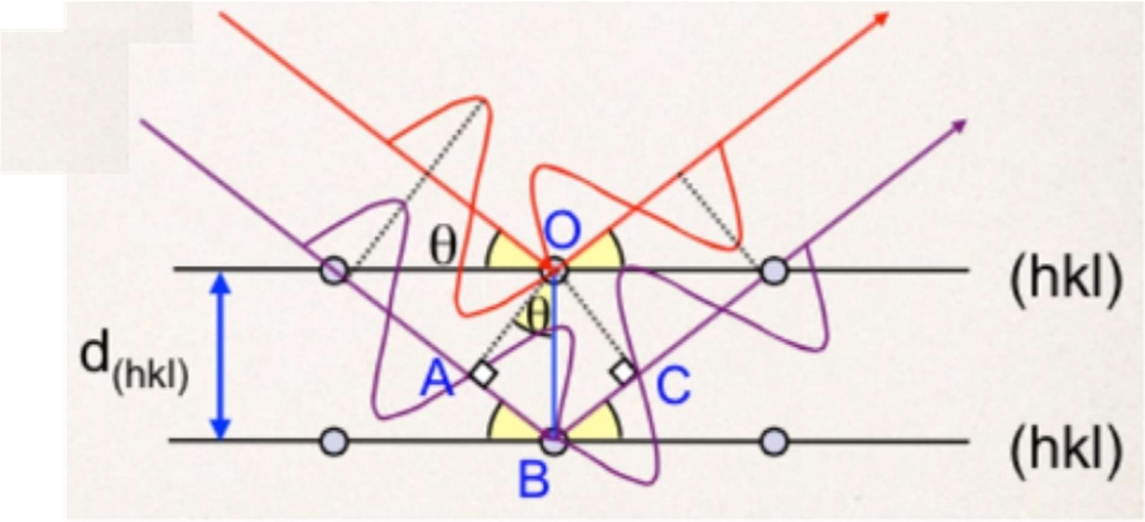

Figure 2.7: Pictorial representation of Bragg's Law reproduced from N. Reeves-McLaren [22].

$$n\lambda = 2d\ sin\ \theta \qquad \textit{Equation 2.1}$$

Where: *n* is the order of reflection or path difference, generally for lab sources this is 1,

λ is the wavelength,

d is the distance between crystal planes,

and θ is the diffraction angle

Bragg's law can be used to predict the angle at which the X-rays are diffracted, based on the unit cell parameters of a material. Using a detector to measure the angles at which diffracted peaks are observed gives a characteristic pattern for a material [26].

To match the position of the peaks and the relative intensities, phase analysis is required. This work uses software called PDF4+, which is released by the International Centre for Diffraction Data (ICDD).

2.4.4: Scanning Electron Microscope (SEM)

The resolution of optical microscopes is limited by the use of visible light, which allows viewing up to approximately 200 nm [27]. Utilising electrons which have much smaller wavelengths has allowed samples to be imaged at a much higher magnification, along with a better depth of field and focus.

Scanning electron microscopes (SEM) use a fine beam of high energy electrons instead of light to scan the surface of a sample, the electrons interact with the atoms on the surface and reveal information regarding the morphology, chemical composition and crystalline structure [28].

Although SEM produces an image that is easily interpreted by the human eye it is important to note that acquiring the image is significantly different from an optical image. Where the human eye immediately observes a full image, the SEM uses an electron beam which is scanned in a raster pattern to obtain an image [29].

The electrons interact with the solid sample and produce a variety of signals, including back scattered electrons (BSE), secondary elections (SE) and X-rays [30].

The interaction volume of the sample usually takes the shape of a water droplet as seen in Figure 2.8 and expands approximately 100 nm – 5 µm below the surface. The interaction volume is dependent on the energy of the electrons hitting the sample, and the density and the atomic number of the sample [28].

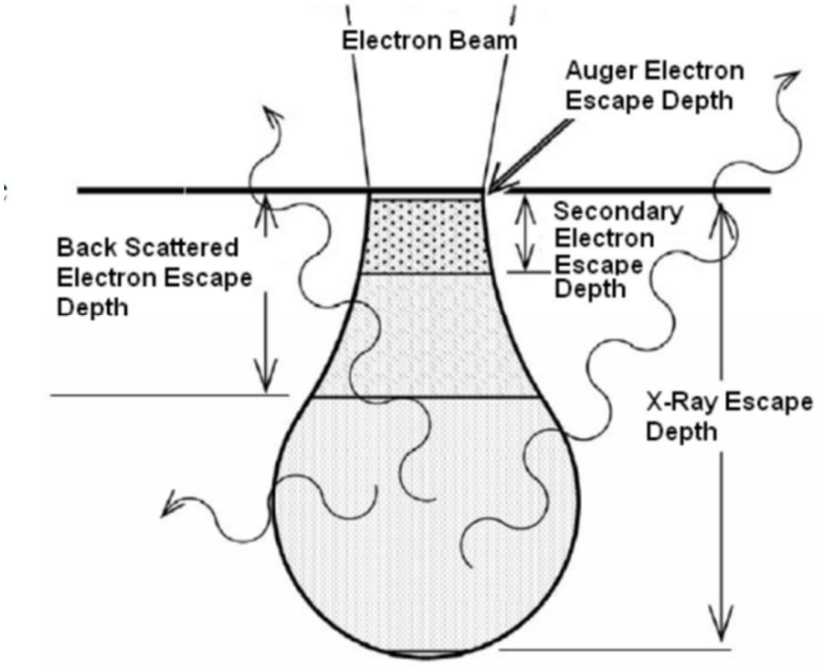

Figure 2.8: Schematic explaining the interaction volume and the signals that are detected in an SEM; reproduced from Hafner [28].

When energy is exchanged with the surface it can occur in numerous different ways, leading to different signals being produced. Secondary electrons are usually low energy electrons emitted from the K shell of the atoms of the specimen via inelastic scattering. As these electrons are low energy they are used to image within a few nanometres of the surface of the sample and can give information on the topology. If the sample is planar it is possible for the electrons to 'escape' between the sample

and the detector, but a peak in the sample area will result in a smaller distance between the sample and the detector and therefore there is less likelihood of the secondary electrons 'escaping'. Therefore, elevated surfaces will appear brighter [29].

Back scattered electrons (BSE) are reflected out of the interaction volume by elastic scattering with the atoms within the sample, the electron beam penetrates deeper than the depth from which secondary electrons can escape and therefore the image is less resolved. It is possible to use BSE for analytical purposes; as heavy atoms backscatter more strongly they appear brighter. As contrast is prevalent between different elements this gives an easy and quick method to identify different chemical compositions before X-ray analysis is performed [31]. Figure 2.9 shows a titanium wire wrapped around a nickel wire imaged via secondary electrons (a), which shows better resolution, and back scattered electrons (b) which show a contrast between the titanium and nickel wires; nickel appears brighter as it has a higher atomic number [32].

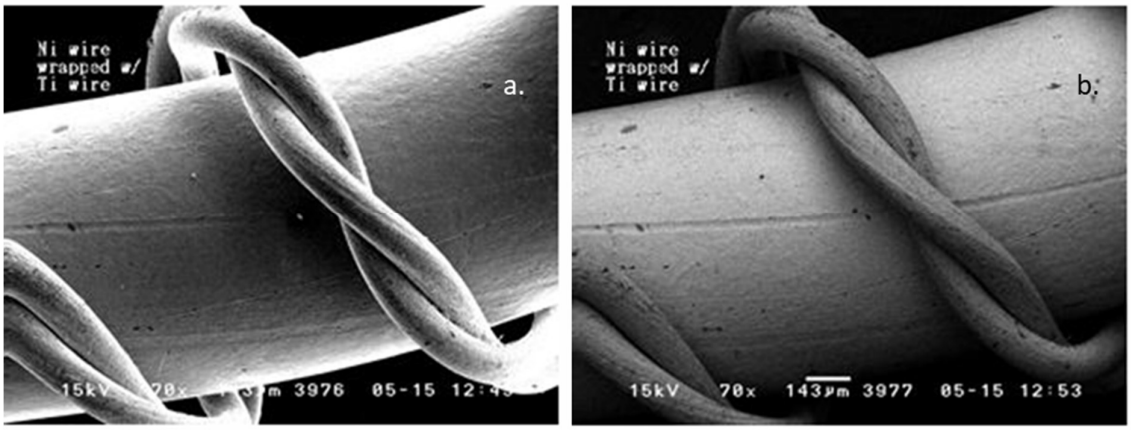

Figure 2.9: The same sample imaged with secondary electrons (a) compared to back scattered electrons (b) (Imaged reproduced from Anderson Materials) [32].

It is possible for the electron beam to remove an inner shell electron resulting in a higher energy electron to fill the shell and emit X-rays. As each element has a characteristic X-ray signal, it is possible to use this to map the compositions and estimate the abundance of each element. This allows for the composition of a surface to be mapped, highlighting key chemical changes that have taken place if these resulted in differences in composition [30].

In addition to the high magnifications that can be obtained from SEM, sample preparation is also minimal. Samples that are conductive only require mounting and polishing, whereas samples which are not electrically conductive require coating with an electrically conductive material, which prevents accumulation of electrostatic charge that can interfere with data acquisition [30].

The scanning electron microscope consists of an electron source, numerous lenses, sample stage, detectors for signals of interest as shown in Figure 2.10.

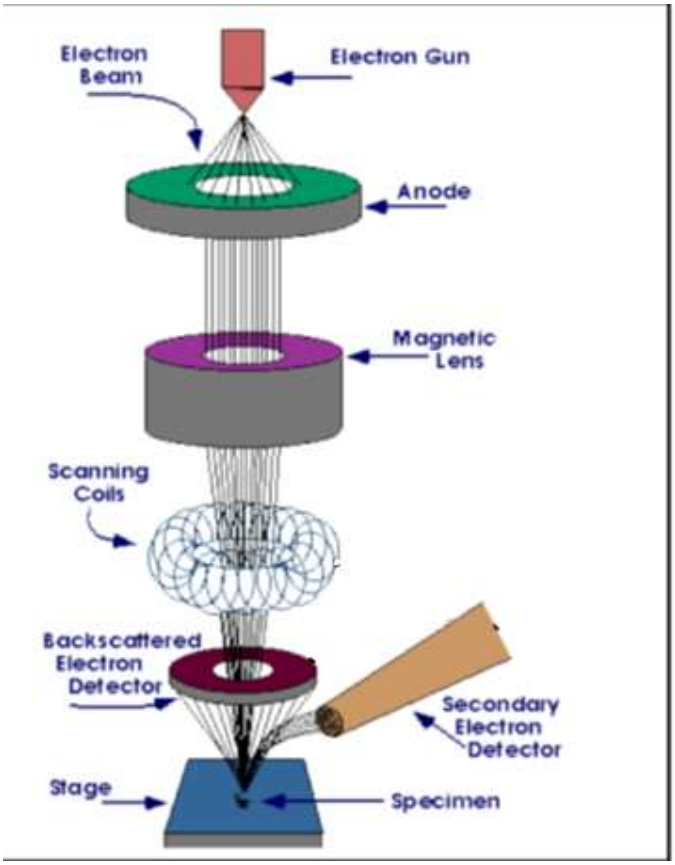

Figure 2.10: Schematic of an SEM, adapted from Maurya et al. [33].

In many SEMs the source of electrons is a thermionic gun, where thermoelectrons are emitted from a tungsten wire filament (cathode) by heating to approximately 3000 K, similar to the method used to generate X-rays in a diffractometer. These electrons are gathered as a beam and accelerated on to the sample.

Electromagnetic lenses are utilised to focus the electron beam, firstly onto a condenser lens, which converges the beam onto the objective aperture. There can be multiple condenser lenses to ensure a thin beam. The objective aperture focuses the beam onto the sample, whilst scan coils move the beam in a raster pattern to obtain the image [29, 33].

Finally, there are numerous different detectors that can be positioned around the sample to collect signals of interest.

Although it is possible to view images relatively quickly at high magnification with little sample preparation there are some limitations to the SEM. For example, usually a vacuum is required as electrons do not move freely through air, although there are some exemptions to this, and X-ray analysis cannot detect light elements such as hydrogen, helium and lithium [30].

This work uses a Hitachi TM3030 desktop SEM with three separate observation modes (5 kV, 15 kV and EDX), with a magnification ranging from 15-30000x; this work usually used magnifications between 40x and 2000x [34].

2.5: Conclusions

This chapter has given an overview of the methods for preparing, testing and analysing the four materials; stainless steel 316L, stainless steel 304L, LDX2101 and iron in molten chlorides. The technique used to prepare the two different eutectic salt mixtures is also outlined.

Literature Cited

1. J.R. Davis, *Stainless Steels*. ASM Specialty Handbook (R) 1999: ASM International.
2. J.R. Keiser, J.H. Devan, and D.L. Manning, *The corrosion resistance of type 316 stainless steel to Li_2BeF_4*. 1977, Oak Ridge National Laboratory.
3. J.R. Reiser, J.H. DeVan, and E.J. Lawrence, *Compatibility of molten salts with type 316 stainless steel and lithium.* Journal of Nuclear Materials, 1979. **85**: p. 295-298.
4. M. Clugston and R. Flemming, *Advanced Chemistry*. 2000, Oxford: Univ. Press.
5. C.K. Dyer, P.T. Moseley, Z. Ogumi, D.A.J. Rand, and B. Scrosati, *Primary Batteries- Reserve Systems: Thermally Activated Batteries: Lithium*, in *Encyclopedia of Electrochemical Power Sources*, J. Garche, Editor. 2009, Elsevier Science.
6. D.S. Coleman and P.D.A. Lacy, *The phase equilibrium diagram for the KCl-NaCl system.* Materials Research Bulletin, 1967. **2**(10): p. 935-938.
7. P.-L. Lin, Pelton, A. D. and Bale, C. W, *Computation of ternary molten salt phase diagrams.* Journal of the American Ceramic Society, 1979. **62**: p. 414-422.
8. Sigma Aldrich, *Sodium Chloride MSDS*. 2013.
9. Alfa Aesar. *A10531 Lithium chloride, anhydrous, 98+%*. 2017 [Accessed on 05-07-2018]; Available from: https://www.alfa.com/en/catalog/A10531/.
10. Alfa Aesar. *A11662 Potassium chloride, 99%*. 2017 [Accessed on 05-07-2018]; Available from: https://www.alfa.com/en/catalog/A10531/.
11. Buehler, *Application Guide: Polishing*. 2015: USA.
12. K. Sridharan and T.R. Allen, *Corrosion in Molten Salts* in *Molten Salts Chemistry*, H. Groult and F. Lantelme, Editors. 2013, Elsevier: Oxford. p. 241-267.
13. L.S. Richardson, D.C. Vreeland, and W.D. Manly, *Corrosion of Molten Fluorides.* Oak Ridge National Laboratory, 1952. **ORNL-1491**.
14. C.B. Boss and K.J. Fredeen, *Concepts, Instrumentation and Techniques in Inductively Coupled Plasma Optical Emission Spectrometry*. 2004, Conneticut: PerkinElmer Life and Analytical Sciences.
15. J.W. Olesik, *10.9 - ICP-OES: Inductively Coupled Plasma-Optical Emission Spectroscopy*, in *Encyclopedia of Materials Characterization*. 1992, Butterworth-Heinemann: Boston. p. 633-644.

16. M. Thompson and J.N. Walsh, *Handbook of Inductively Coupled Plasma Spectrometry*. 1994: Blackie Academic and Professional
17. P. Atkins and J.D. Paula, *Atkins' Physical Chemistry*. 2006: Oxford University Press.
18. R. Thomas, *Practical Guide to ICP-MS: A Tutorial for Beginners*. 2013: CRC Press.
19. M. Thompson, *CHNS elemental analysers* Analytical Methods Committee Technical Briefs, Editor. April 2008, The Royal Society of Chemistry.
20. F. Rouessac and A. Rouessac, *Chemical Analysis: Modern Instrumentation Methods and Techniques*. 2nd Edition ed. 2007: John Wiley and Sons, Ltd.
21. A.R. West, *Solid State Chemistry and its Applications*. 1984: John Wiley and Sons.
22. N. Reeves-McLaren, *MAT6665: Diffraction Lecture Notes*. 2014, Department of Materials Science and Engineering, University of Sheffield.
23. Bruker, *D2 Phaser. Diffraction Studies*. 2009.
24. C. Suryanarayana and M.G. Norton, *X-Ray Diffraction: A Practical Approach*. 2013: Springer Science & Business Media.
25. Oxford Instruments PLC, *Caring for the Beryllium Window of an X-ray Tube*, O.I. PLC, Editor. 2015.
26. K. DeWitt, J. Batson, M. Witkowski, N. Ranieri, and L. Richards-Waugh, *X-Ray Powder Diffraction Method Development and Validation for the Identification of Counterfeit Pharmaceuticals*, in *Forensic Science*. 2016, Marshall University.
27. Mary Jones, Richard Fosbery, Jennifer Gregory, and D. Taylor, *Cambridge International AS and A Level Biology Coursebook*. 4th Edition ed. 2014: Cambridge University Press.
28. B. Hafner, *Scanning Electron Microscopy Primer*. 2007, Characterization Facility, University of Minnesota—Twin Cities.
29. D. Chescoe and P.J. Goodhew, *The Operation of Transmission and Scanning Electron Microscopes*. Royal Microscopical Society- Microscope Handbooks. Vol. 20. 1990: Oxford Science Publications.
30. B. Cheney, *Introduction to Scanning Electron Microscopy*. San Jose State University.
31. J. Bert, *A Review of Scanning Electron Microscopy with Spin Analysis*. 2007.
32. Anderson Materials Evaluation. *SEM Illustrative Example: Secondary Electron and Backscatter Electron Images*. 2017 30th August 2017]; Available from: http://www.andersonmaterials.com/sem/sem-secondary-backscatter-images.html.
33. S. Maurya and A. Paunikar, *Automotive Fasteners Defects and Failure Analysis*. 2016.
34. Hitachi, *Hitachi tabletop microscope TM3030*, Hitachi High-Technologies Corporation, Editor. 2013.